






Article

# Numerical Analysis of an Overtopping Wave Energy Converter Subjected to the Incidence of Irregular and Regular Waves from Realistic Sea States

Ricardo G. Hubner <sup>1</sup>, Cristiano Fragassa <sup>2,\*</sup> , Maycon da S. Paiva <sup>3</sup>, Phelype H. Oleinik <sup>1</sup> , Mateus das N. Gomes <sup>4</sup> , Luiz A. O. Rocha <sup>1</sup>, Elizaldo D. dos Santos <sup>1</sup> , Bianca N. Machado <sup>5</sup> and Liércio A. Isoldi <sup>1</sup> 

<sup>1</sup> School of Engineering, Federal University of Rio Grande (FURG), Italia Av., km 8, Rio Grande 96203-900, RS, Brazil

<sup>2</sup> Department of Industrial Engineering, University of Bologna, Viale Risorgimento 2, 40136 Bologna, Italy

<sup>3</sup> Department of Pure and Applied Mathematics, Federal University of Rio Grande do Sul, Bento Gonçalves Av., 9500, Porto Alegre 91509-900, RS, Brazil

<sup>4</sup> Federal Institute of Paraná (IFPR), Antônio Carlos Rodrigues Av., 453, Paranaguá 83215-750, PR, Brazil

<sup>5</sup> Interdisciplinary Department, Federal University of Rio Grande do Sul (UFRGS), RS 030, 11.700-km 92 Emboaba, Tramandaí 95590-000, RS, Brazil

\* Correspondence: cristiano.fragassa@unibo.it; Tel.: +39-347-697-4046

**Abstract:** The present study aims to evaluate the difference in the fluid-dynamic behavior of an overtopping wave energy converter under the incidence of irregular waves based on a realistic sea state when compared to the incidence of regular waves, representative of this sea state. Thus, the sea data of three regions from the Rio Grande do Sul coast, Brazil, were considered. Fluent software was employed for the computational modeling, which is based on the finite volume method (FVM). The numerical generation of waves occurred through the imposition of the velocity boundary conditions using transient discrete values through the WaveMIMO methodology. The volume of fluid (VOF) multiphase model was applied to treat the water–air interaction. The results for the water amount accumulated in the device reservoir showed that the fluid-dynamic behavior of the overtopping converter has significant differences when comparing the two proposed approaches. Differences up to 240% were found for the water mass accumulated in the overtopping device reservoir, showing evidence that the results can be overestimated when the overtopping device is analyzed under the incidence of the representative regular waves. Furthermore, for all studied cases, it was possible to approximate the water volume accumulated over time in the overtopping reservoir through a first-degree polynomial function.

**Keywords:** wave energy; WaveMIMO methodology; realistic sea state; computational modeling



**Citation:** Hubner, R.G.; Fragassa, C.; Paiva, M.d.S.; Oleinik, P.H.; Gomes, M.d.N.; Rocha, L.A.O.; Santos, E.D.d.; Machado, B.N.; Isoldi, L.A. Numerical Analysis of an Overtopping Wave Energy Converter Subjected to the Incidence of Irregular and Regular Waves from Realistic Sea States. *J. Mar. Sci. Eng.* **2022**, *10*, 1084. <https://doi.org/10.3390/jmse10081084>

Academic Editor: Remo Cossu

Received: 6 July 2022

Accepted: 5 August 2022

Published: 8 August 2022

**Publisher's Note:** MDPI stays neutral with regard to jurisdictional claims in published maps and institutional affiliations.



**Copyright:** © 2022 by the authors. Licensee MDPI, Basel, Switzerland. This article is an open access article distributed under the terms and conditions of the Creative Commons Attribution (CC BY) license (<https://creativecommons.org/licenses/by/4.0/>).

## 1. Introduction

According to Fontana et al. [1], the demand of humanity for energy is amplified by population growth in underdeveloped countries and by the high energy consumption of developed countries. Therefore, as stated in REN21 [2], investment and the capacity to produce energy from renewable sources have increased annually. For example, these sources already accounted for 26.20% of the electricity consumed in the world in 2018. In this context, as estimated by Gunn and Stock-Williams [3], the global wave energy potential is approximately 2.11 TW. According to Espindola and Araújo [4], the estimated total annual potential for the Brazilian coast is 89.97 GW, with the southern region having the highest wave energy potential in the country, reaching an average of 20.63 kW/m per wavefront.

Among the different types of existing wave energy converters (WECs), the overtopping device stands out for being a robust and resistant equipment. Its operational principle is

based on a partially submerged structure that uses a ramp to drive water to a reservoir. The waves overtop the ramp and enter the reservoir, where the water is temporarily stored before its return to the sea via hydro turbines, generating electricity [5]. Computational modeling plays an important role for the hydrodynamic behavior study of the overtopping devices through approaches that consider the incidence of regular or irregular waves, allowing for the prediction of its capacity to convert the wave energy into electricity.

Concerning the incidence of regular waves, Jungrungruentaworn and Hyun [6] developed a numerical investigation evaluating the influence of the overtopping slot width on the hydraulic performance of the device. Han et al. [7] carried out a numerical study of a two-stage overtopping WEC (i.e., two ramps and two reservoirs), comparing the results with those experimentally obtained by Liu et al. [8]. Martins et al. [9] performed a geometric evaluation of the overtopping device employing the Constructal Design, considering two degrees of freedom: the ratio between height and length of the ramp and the device depth. In turn, the incidence of irregular waves in overtopping WECs has been done through the Joint North Sea Wave Project (JONSWAP) wave spectrum, which simulates random waves. Palma et al. [10] presented numerical studies on the hydraulic performance of an overtopping breakwater for energy conversion (OBREC), being a breakwater with an integrated overtopping device. Di Lauro et al. [11] also studied an OBREC employing the JONSWAP spectrum, developing its stability analysis by combining model scale experiments and numerical simulations that use the IH2VOF model, which is based on the volume-averaged Reynolds-averaged Navier–Stokes (VARANS) equations combined with the VOF method. Additionally, Di Lauro et al. [12] performed numerical simulations based on the VARANS equations, aiming to investigate the hydraulic performance and structural stability of the innovative OBREC-V, and concluded that the proposed non-conventional geometry can promote significant improvements in wave energy extraction, reduction of the wave reflection, and hydraulic stability when compared with the traditional OBREC design. More recently, Martins et al. [13], also applying the JONSWAP spectrum, developed a numerical study on an overtopping device with one and two ramps incorporated into a real breakwater, performing a geometric evaluation through the Constructal Design method. It should be highlighted that one can find several other studies addressing the overtopping devices and OBRECs with different approaches and goals, such as the studies by Liu et al. [14], Barbosa et al. [15], Contestabile et al. [16], and Mariani et al. [17].

In view of this, the present work uses computational modeling to reproduce the operational principle of an overtopping WEC in order to analyze numerically its fluid-dynamic behavior when subjected to regular and irregular waves based on realistic sea states. Thereunto, three different points located 2000 m off the coast of Rio Grande do Sul state were considered, in the municipalities of Rio Grande (RG), Santa Vitória do Palmar (SVP), and Tavares (TV), in southern Brazil. To do so, representative regular waves and realistic irregular waves of each sea state were generated through the WaveMIMO methodology [18] application. In both approaches, a real-scale wave channel with a numerical beach was considered, in which the overtopping WEC is inserted.

## 2. Ocean Wave Energy and Its Conversion

The analysis of the wave energy resource is an essential requisite for the strategic planning of its adequate usage, as well as for the design of WECs [19]. In a general way, the waves start as small ripples that become larger due to the sustained transfer of energy from wind. If the wind keeps blowing long enough, the waves reach a limit beyond which their existence no longer depends on the continued wind action. In that case, the waves are regarded as being fully developed. For a wave to become fully developed, it depends on the wind velocity and the distance (or fetch) over which the wind is blowing. Nonetheless, if the wind stops, these waves will continue to propagate for large distances with practically no energy loss, being defined as swell waves since the wind that caused their generation is no longer present [5].

Based on the above, one can classify ocean waves into the following two categories: wind waves (generated by local winds; will dissipate if wind action ceases) and swell waves (away from their generation zone; do not depend on wind action to propagate) [5]. In other words, wind waves can be considered to be young waves that grow or are in equilibrium with the local winds, while swell waves can be regarded as waves that originated elsewhere, having the ability to propagate over long distances [20]. Despite this classification, wind waves and swell waves are basically two extremes of a continuum of waves. In fact, all waves are generated due to a previous wind action and subject to the effect of the local wind [5].

Regarding the conversion of ocean wave energy, several physical operating principles are studied and tested for the WEC devices. According to Pecher and Kofoed [5], these devices can be classified into the following categories: oscillating water column (OWC), with a fixed or floating structure; oscillating, floating, or submerged bodies; and overtopping, with a fixed or floating structure. However, the above classifications do not cover all the studied WECs, which is the case of the submerged horizontal plate device [21,22].

The WEC power performance, in theory, benefits from the incidence of wind waves that are steep and provide larger and/or more frequent interactions with the device. In turn, swell waves have longer periods, resulting in less frequent interactions with the WECs [5]. In addition, it is believed that swell waves can be considered detrimental for the WECs, because they affect the wave height, wave period, and regularity of the wave climate, resulting in an irregular energy production pattern [23]. However, there is no adequate data to estimate the extra energy that can be generated by the swells. Experimental tests performed by Kralli et al. [24] indicated that an OBREC can achieve a performance that is improved by 20% due to the incidence of swell waves.

To improve the studies on wave energy conversion, researchers have carried out several numerical investigations regarding the propagation of regular and irregular waves. Some examples of studies on the generation of regular waves can be seen in Zabihi et al. [25], who compared two software to generate numerical waves, Fluent and Flow-3D. In addition, the use of a ramp at the end of the channel was investigated as a means to dissipate the wave energy. Machado et al. [26] presented a method for generating regular waves using the Fluent software, inserting transient discrete data as the velocity inlet boundary conditions on the wave channel. Machado et al. [27] tested two ways to generate regular waves on a numerical wave tank: using a piston wavemaker and using the prescribed velocity boundary conditions. As for irregular waves, there are studies, such as Finnegan and Goggins [28], that have studied the generation of irregular waves on a real scale using the Fluent software. Higuera et al. [29,30] developed and validated a numerical methodology for realistic wave generation associated with active wave absorption, based on the linear shallow-water theory, in OpenFOAM software. Machado et al. [18] presented the WaveMIMO methodology, which allows the numerical simulation of realistic sea waves based on the imposition of transient discrete data as a prescribed velocity boundary condition using Fluent software.

### 3. Data and Methodology

This section presents the aspects necessary for the numerical simulation of the overtopping WEC subjected to the incidence of representative regular waves and realistic irregular waves from the three studied coastal regions located in the southern Brazil.

#### 3.1. Mathematical and Numerical Modeling

The numerical simulations of the present investigation were carried out using the ANSYS Fluent software, which is a computational fluid dynamics (CFD) package based on the finite volume method (FVM). The FVM divides the domain of interest into several elementary volumes and performs a conservation balance of properties for each elementary volume to obtain the corresponding approximate equation [31,32].

The volume of fluid (VOF) multiphase model was used to deal with the two-phase flow of air and water. This methodology was developed by Hirt and Nichols [33] allowing the adequate treatment of the water–air interaction, because assumes that the volume occupied by one phase cannot be occupied by the other phase. To represent which phase is present in each volume, the model calculates the volumetric fraction ( $\alpha$ ). Thus,  $\alpha$  varies between 0 and 1 for each phase ( $\alpha_{water}$  and  $\alpha_{air}$ ), where 0 indicates that the measured phase is not present and 1 indicates that only that phase is present in the control volume. Therefore

$$\alpha_{air} = 1 - \alpha_{water} \tag{1}$$

Furthermore, still according to Hirt and Nichols [33], when the VOF model is applied, the momentum and continuity equations are solved for each cell of the computational domain, and the volumetric fraction ( $\alpha$ ) is calculated for each control volume on the domain through the transport equation. Thus, in agreement with Schlichting [34] the model is composed by the Navier–Stokes equation for the water–air mixture:

$$\frac{\partial(\rho \vec{v})}{\partial t} + \nabla \cdot (\rho \vec{v} \vec{v}) = -\nabla p + \nabla \cdot (\mu \bar{\bar{\tau}}) + \rho \vec{g} + S \tag{2}$$

continuity equation:

$$\frac{\partial(\rho)}{\partial t} + \nabla \cdot (\rho \vec{v}) = 0 \tag{3}$$

and volumetric fraction transport equation:

$$\frac{\partial(\rho\alpha)}{\partial t} + \nabla \cdot (\alpha \vec{v}) = 0 \tag{4}$$

where  $\rho$  is the fluid density ( $\text{kg}/\text{m}^3$ );  $t$  is the time (s),  $\vec{v}$  is the velocity vector ( $\text{m}/\text{s}$ );  $p$  is the static pressure (Pa);  $\mu$  is the viscosity ( $\text{kg}/(\text{m}\cdot\text{s})$ );  $\bar{\bar{\tau}}$  is the stress deformation tensor ( $\text{N}/\text{m}^2$ ); and  $\vec{g}$  is the gravity acceleration vector ( $\text{m}/\text{s}^2$ ). Still,  $S$  is the damping sink term and refers to the numerical beach, a tool used to avoid the effect of wave reflection at the end of the wave channel, given by [35,36], as follows:

$$S = -\left[ C_1\rho V + \frac{1}{2}C_2\rho|V|V \right] \left( 1 - \frac{z - z_{fs}}{z_b - z_{fs}} \right) \left( \frac{x - x_s}{x_e - x_s} \right)^2 \tag{5}$$

where  $C_1$  and  $C_2$  are the linear and quadratic damping coefficients, respectively;  $V$  is the velocity along the  $z$ -direction;  $z$  is the vertical position (m);  $z_{fs}$  and  $z_b$  are the vertical positions of the free surface and bottom, respectively;  $x$  is the horizontal position (m); and  $x_s$  and  $x_e$  are the horizontal positions of the beginning and end of the numerical beach, respectively. In concordance with Lisboa et al. [36], the damping coefficients adopted are  $C_1 = 20$  and  $C_2 = 0$ .

### Realistic Sea State Data and Wave Generation

The realistic data used for the generation of waves in the present study come from the spectral model TOMAWAC (TELEMAC-based operational model addressing wave action computation) and consist of a set of points in space, where each point is composed of a directional spectrum of waves that vary over time. Such data are obtained by solving the equation that represents the general situation of the wave propagation in an unstable and nonhomogeneous medium, given by [37], as follows:

$$\frac{\partial N}{\partial t} + \frac{\partial(\dot{x}N)}{\partial x} + \frac{\partial(\dot{z}N)}{\partial z} + \frac{\partial(\dot{k}_x N)}{\partial k_x} + \frac{\partial(\dot{k}_z N)}{\partial k_z} = Q(k_x, k_z, x, z, t) \tag{6}$$



where  $N$  represents the directional spectrum of wave action density ( $\text{m}^2/\text{Hz}/\text{rad}$ );  $k_x$  is the component  $x$  of the wave number vector ( $\text{m}^{-1}$ );  $k_z$  is the component  $z$  of the wave number vector ( $\text{m}^{-1}$ ); and  $Q$  is the source term ( $\text{m}^2/\text{rad}$ ).

In the present paper, three points along the coast of the state of Rio Grande do Sul, located in southern Brazil, were considered. These points are 2000 m away from the coast of the municipalities of Rio Grande (RG), Santa Vitória do Palmar (SVP), and Tavares (TV). Figure 1 represents the computational domain used for the simulation of the sea state of these points, through the TOMAWAC software.

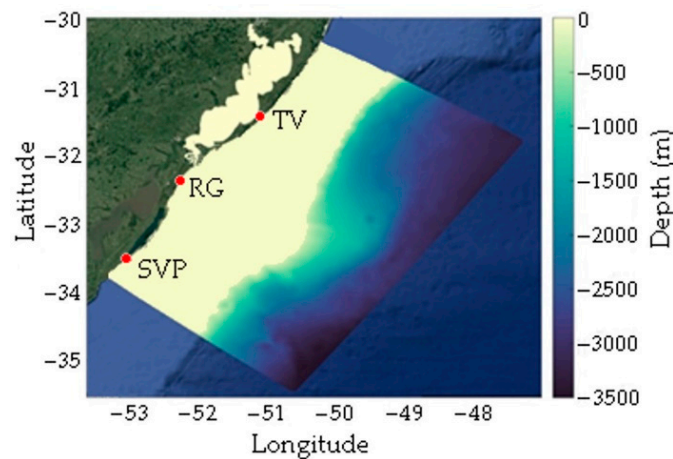


**Figure 1.** Computational domain used in the TOMAWAC software to obtain the sea state data.

The generation of the realistic irregular waves in this study occurred through the WaveMIMO methodology [18], which was validated and verified in Maciel et al. [38]. Such methodology consists of imposing discretized orbital velocity profiles, horizontal and vertical, of the wave propagation as boundary conditions based on realistic sea state data.

As explained in Machado et al. [14] and Oleinik et al. [39], after the realistic data are obtained, the inverse Fourier transform is used to convert them into free-surface elevation time series. Thus, it is possible to approximate the spectral data by a finite sum of monochromatic waves, described individually according to the linear wave theory, as [40,41]:

$$\eta = A \cos(kx - \omega t), \tag{7}$$

where  $\eta$  is the water free-surface elevation (m);  $A$  is the wave amplitude (m);  $k$  is the wave number ( $\text{m}^{-1}$ ); and  $\omega$  is the angular frequency (Hz). Furthermore, the wave number and angular frequency are given, respectively, as:

$$k = \frac{2\pi}{\lambda}, \tag{8}$$

$$\omega = \frac{2\pi}{T}, \tag{9}$$

where  $\lambda$  is the wavelength (m) and  $T$  is the wave period (s).

Thus, by deriving the free-surface elevation equation for each coordinate axis, it is possible to obtain horizontal ( $u$ ) and vertical ( $w$ ) orbital velocity profiles of wave propagation given, respectively, by:

$$u = \omega A \frac{\cosh h(kz + kh)}{\sinh h(kh)} \cos(kx - \omega t) \tag{10}$$

$$w = \omega A \frac{\sinh h(kz + kh)}{\sinh h(kh)} \sin(kx - \omega t) \tag{11}$$

where  $h$  is the water depth (m).

In addition, it is important to highlight that the regular waves employed in this study are representatives of the addressed realistic sea states. Thus, their characteristics are determined from the histograms of the frequency of occurrence of each wave spectrum throughout 2014, which combine the significant height ( $H_s$ ) and peak period ( $T_p$ ) of the spectrum, and can be seen in Figures 2–4, respectively, for the RG, SVP, and TV regions (see Figure 1).

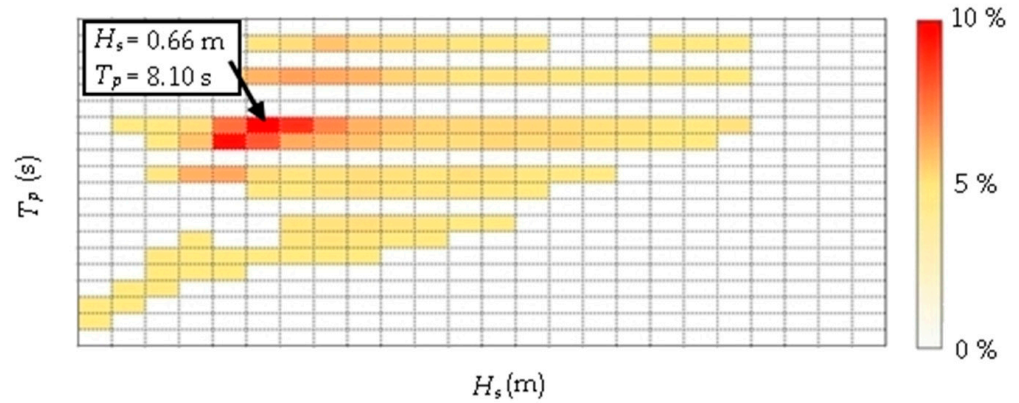


Figure 2. Histogram of frequency of occurrence of sea state for the point referring to RG.

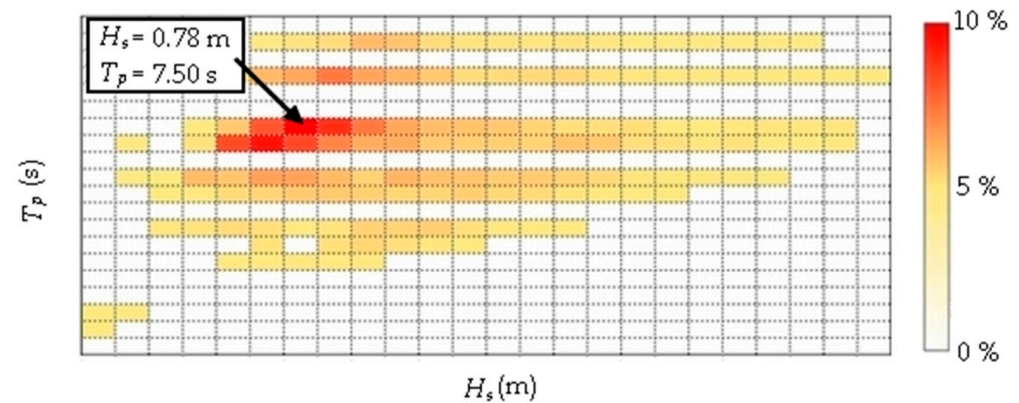


Figure 3. Histogram of frequency of occurrence of sea state for the point referring to SVP.

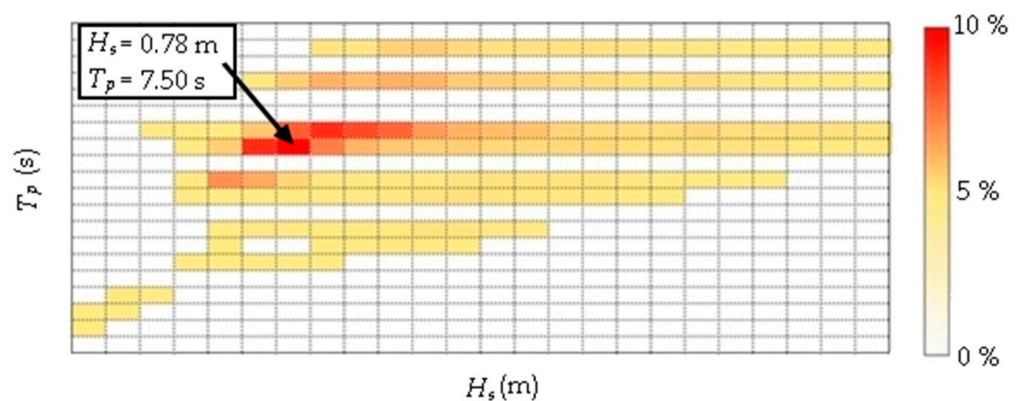


Figure 4. Histogram of frequency of occurrence of sea state for the point referring to TV.

After obtaining the most frequent significant height and peak period of each coastal region, the wavelengths ( $\lambda$ ) were calculated using the dispersion relation [41]:

$$\omega^2 = gk \tanh kh. \tag{12}$$

Hence, in Table 1, the characteristics adopted for the representative regular waves of each studied region are presented.

**Table 1.** Characteristics of representative regular waves.

Point	Height— <i>H</i> (m)	Period— <i>T</i> (s)	Wavelength— $\lambda$ (m)
RG	0.66	8.10	85.98
SVP	0.78	7.50	68.48
TV	0.78	7.50	68.48

Thus, according to Chakrabarti [42], the regular waves considered in this study are second-order Stokes waves. Therefore, according to Dean and Dalrymple [41], the free-surface elevation of the water caused by these waves, and the horizontal and vertical velocity components, can be analytically described, respectively, by:

$$\eta = A \cos(kx - \omega t) + \frac{(2A)^2 k \cos h(kh)}{16 \sin h^3(kh)} [2 + \cos h(2kh)] \cos[2(kx - \omega t)], \quad (13)$$

$$u = Agk \frac{\cos h(kz + kh)}{\omega \cos h(kh)} \cos(kx - \omega t) + A^2 \omega k \frac{\cos h[2k(h + z)]}{\sin^4(kh)} \cos[2(kx - \omega t)], \quad (14)$$

$$w = Agk \frac{\sin h(kz + kh)}{\omega \sin h(kh)} \sin(kx - \omega t) + A^2 \omega k \frac{\sin h[2k(h + z)]}{\cos^4(kh)} \sin[2(kx - \omega t)]. \quad (15)$$

Aiming to apply the WaveMIMO methodology for the generation of these regular waves, as in Chakrabarti [42], the components of the wave propagation velocity vector were extracted in the horizontal (*u*) and vertical (*w*) directions for each coastal region. Therefore, a time step of  $\Delta t = 0.05$  s was used, which according to Liu et al. [43] guarantees numerical accuracy because  $\Delta t \leq T/50$ .

Finally, Table 2 presents precise information regarding the location of the selected points (see Figure 1) as well as the moment to which the data refer.

**Table 2.** Characteristics of each point selected for the study.

Point	Date	Time (h)	Geographic Location	Depth— <i>h</i> (m)
RG	8 September 2014	8.25	−52° 17′ 47.25′ W, −032° 22′ 30.95′ S	9.52
SVP	31 July 2014	18.5	−53° 04′ 29.27′ W, −033° 32′ 42.47′ S	11.09
TV	24 February 2014	12.75	−51° 06′ 20.37′ W, −031° 27′ 7.97′ S	13.97

### 3.2. Problem Description

The analyzed problem consists of an overtopping WEC inserted into a wave channel and subjected to the incidence of waves that represent different sea states. Therefore, a two-dimensional computational model was developed to simulate the operational principle of the device. It is worth mentioning that the 2-D numerical approach has been widely used for the investigation of WECs [18,21,22,38,43,44], including overtopping devices [6–10,13,15]. This simplification is reasonable especially for the overtopping WEC, since the physical phenomenon that occurred due to the incidence of waves can be adequately approximated as an in-plane problem. Moreover, the 2-D approach is justified if it is taken into account the processing time required for this kind of numerical simulation.

As shown in Figure 5, at the bottom of the left side of the wave channel (dashed green and red line), the prescribed velocity boundary conditions are imposed, which allows for the generation of waves referring to each sea state addressed. Furthermore, the other boundary conditions are as follows: atmospheric pressure (dashed blue line); pressure outlet (orange line), in which a hydrostatic pressure profile is imposed, thereby enabling the

use of the numerical beach (gray region); wall condition (i.e., non-slip and impermeability) at the bottom of the channel, as well as on the overtopping device (black line).

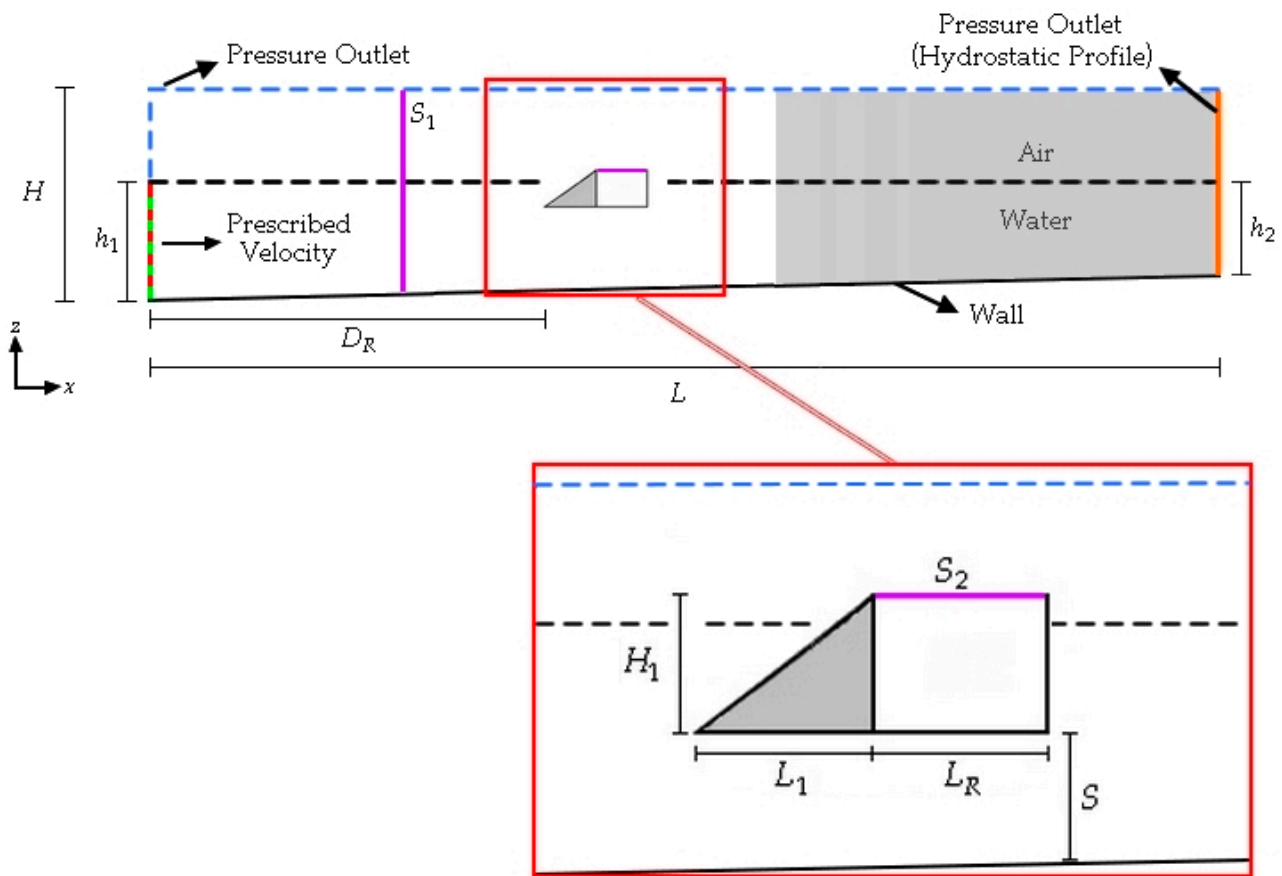


**Figure 5.** Schematic representation of the two-dimensional computational domain of the overtopping device in the wave channel.

It is worth mentioning that for the pressure outlet imposed at the right boundary of the computational domain (orange line, in Figure 5), the outlet pressure was defined by prescribing the free-surface level as a hydrostatic pressure profile, characterizing an open channel flow. From that, the numerical beach is considered as a region with its end surface as the open channel pressure outlet boundary (hydrostatic profile), which is parallel to its initial surface (start line of the gray region in the wave channel, in Figure 5). In addition, the direction of the numerical beach is normal to its initial and end surfaces, with the damping effect increasing gradually from the beginning of the numerical beach until its final boundary [45,46].

Furthermore, the wave channel has a length of  $L = 420$  m and an initial height of  $H = 20$  m. These dimensions were assumed based on the recommendations of Gomes et al. [44], adopting the wavelength of RG and the wave height of SVP and TV (see Table 1) as references. As can be seen in Figure 5, the channel bottom is inclined, following the bathymetric data obtained from nautical charts of the Brazilian Navy’s Directorate of Hydrography and Navigation <sup>1</sup>. Thus, it is highlighted that the depth varies from  $h_1 = 9.52$  m to  $h_2 = 9.15$  m in RG; from  $h_1 = 11.09$  m to  $h_2 = 10.65$  m in SVP; and from  $h_1 = 13.98$  m to  $h_2 = 13.36$  m in TV, where  $h_1$  refers to the depth at the selected point (indicated as  $h$  in Table 2) and  $h_2$  refers to the depth at the point that is 420 m away, in the coast direction.

Regarding the dimensions of the overtopping WEC, the recommendations of Martins et al. [9] were adopted (see Figure 5):  $D_R = 140$  m; ratio  $H_1/L_1 = 0.33$ , with  $H_1 = 7.15$  m and  $L_1 = 21.66$  m;  $L_R = 20$  m; and  $(h_1 - S) = 6.5$  m. Lines  $S_1$  and  $S_2$



(purple lines in Figure 5) represent, respectively, the probes for monitoring the water free-surface elevation, located 120 m from the left side wall of the computational domain, and the mass flow rate, at the entrance of the reservoir. It is worth noting that the boundary conditions, the characteristics of the overtopping device, and the wave channel were kept constant for all simulated cases, with the exceptions being the values of  $h_1$ ,  $h_2$ , and  $S$ , which needed to be altered for each case due to the local bathymetry.

Moreover, for spatial discretization, the computational domain was divided into three distinct regions, as follows: R1 is the wave generation region, with 30 m in length; R2 is the device region, with 151.81 m in length; and R3 is the numerical beach region, starting at  $x_s = 181.81$  m and ending at  $x_e = 420$  m (see Equation (5)), leading to a numerical beach with 238.19 m in length. In Figure 6, it is possible to observe a representation of the mentioned regions of the computational domain.

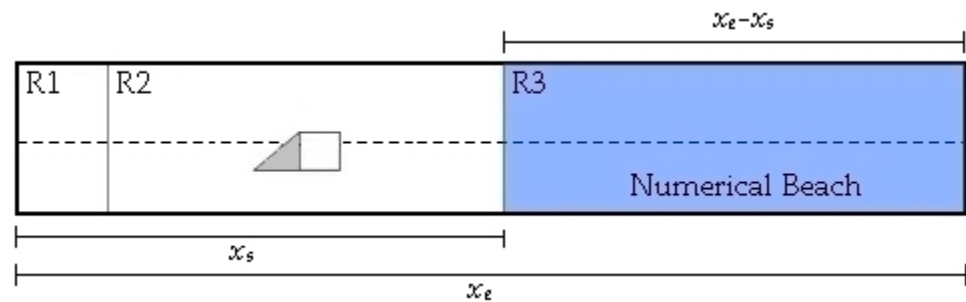


Figure 6. Schematic representation of the computational domain regions.

The R1 region was discretized with an irregular mesh composed by triangles of side  $\Delta x = 0.3$  m, according to Kisner et al. [47]. The R2 region was discretized with a structured mesh, as in Gomes et al. [44], having horizontally 125 computational cells per wavelength defined by a mesh independence test. The R3 region was discretized with quadrilaterals of side  $\Delta x = 0.5$  m, as indicated by Saincher and Banerjee [48]. Figure 7 illustrates the mesh adopted for the computational domain, detailing each mentioned region.

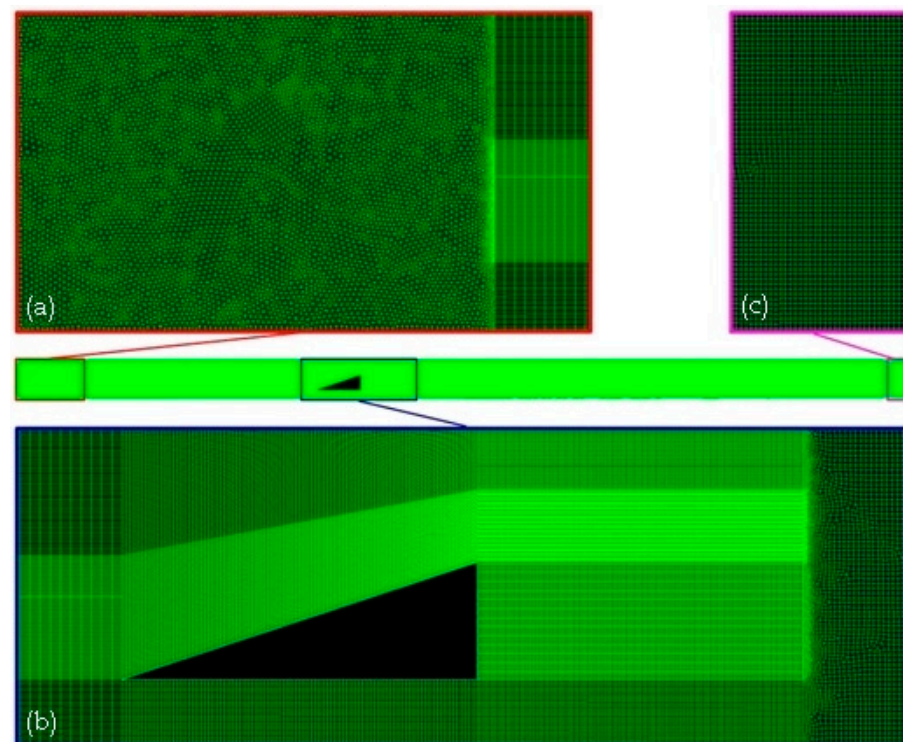
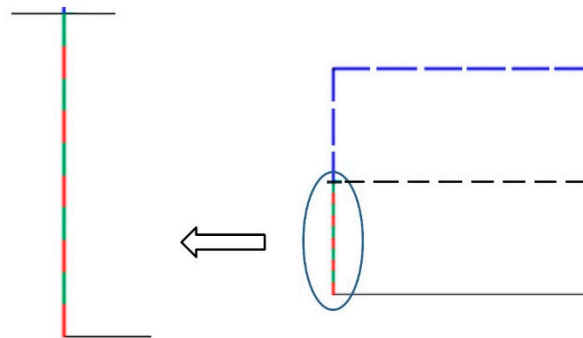


Figure 7. Mesh used, detailing the regions (a) R1; (b) R2; and (c) R3.



As for the temporal discretization, for the representative regular and realistic irregular waves, a time step of  $\Delta t = 0.05$  s was adopted, following the indication from Liu et al. [43] for regular waves and Machado et al. [18] for irregular waves. A total time of 600 s of wave propagation was simulated. Concerning the initial condition, it was assumed that water and air were at rest, while the water depth at the beginning of the wave channel in each case was adopted as being equal to the wave height of the correspondent representative regular wave (see Table 2).

It should be noted that a particularity for applying the WaveMIMO [18] is to subdivide the segment, where the prescribed velocity boundary condition is imposed into smaller segments, 1 m long, as indicated in Machado et al. [26]. Figure 8 illustrates the wave channel inlet region of Figure 5.



**Figure 8.** Imposition region of the prescribed velocity boundary conditions for wave generation through discrete transient data [26].

#### 4. Results

The verification and validation of the WaveMIMO methodology were carried out in Machado et al. [18] and Maciel et al. [38]. Therefore, for the sake of brevity, the verification of the numerical model used in the generation of waves will not be showed in the present paper. Thus, the first results presented are related to the spatial discretization adopted for the R2 region of the computational domain (see Figures 6 and 7). Finally, the results obtained for the three studied coastal regions (see Figure 1) are reported regarding the incidence of regular and irregular waves in the WEC overtopping.

##### 4.1. Mesh Independence Test

Specifically, for the R2 region (see Figures 6 and 7), an investigation was carried out focusing on the spatial discretization to be adopted. It was based on the recommendations indicated in Gomes et al. [44], which used 50 computational cells per wavelength in the horizontal direction. However, to obtain the greatest possible accuracy in the device region, meshes with different refinements in horizontal discretization were tested, as follows: 50, 75, 100, and 125 cells per wavelength.

To compare the performance of the tested meshes, the amount of water that entered the device reservoir due to the incidence of the representative regular waves of RG was monitored through probe  $S_2$ , located at the reservoir entrance (see Figure 5). Thus, Figure 9 presents the relationship between the number of segments per wavelength adopted in the horizontal discretization and the mass of water accumulated in the device reservoir.

As can be seen in Figure 9, there is a tendency to stabilize the results obtained from 75 computational cells per wavelength. Thus, it was decided to use the mesh with 125 cells per wavelength in the R2 region, guaranteeing a more accurate result regarding the amount of water stored in the reservoir due to the incident waves over the overtopping WEC.

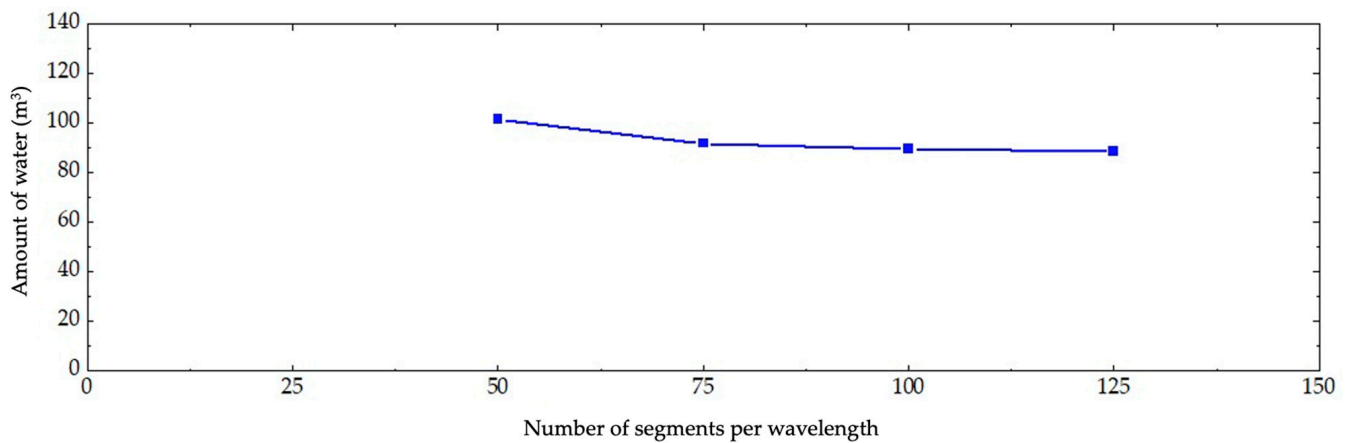


Figure 9. Mesh convergence test for region R2 of the computational domain.

#### 4.2. Incidence of Waves on the Overtopping WEC

The numerical analysis of the operational principle of the overtopping WEC consisted of calculating the amount of water that enters its reservoir. The main objective here was to compare the performance of this device when subjected to realistic irregular waves with its performance under the incidence of representative regular waves, for the three different coastal locations indicated in Figure 1.

Initially, probe  $S_1$  (located at  $x = 120$  m, see Figure 5) was used to monitor the free-surface elevation in the wave channel. Thus, Figures 10–12 illustrate a qualitative comparison between the free-surface elevation that occurred with the representative regular waves and the realistic irregular waves for the sea state that occurred in RG, SVP, and TV, respectively.

From Figures 10–12, as expected, the free-surface elevation caused by the generation of representative regular waves presents constant wave peaks for the three cases. On the other hand, the elevation caused by the generation of realistic irregular waves presents variable wave peaks, sometimes larger, sometimes smaller than those caused by the simulation of regular waves, reproducing in a more accurate way the behavior of the ocean waves.

To determine whether the simplification performed using regular waves adequately represents the fluid-dynamic behavior of the overtopping WEC, the mass of water accumulated in the device reservoir was monitored and compared in each coastal region. A qualitative analysis of the results can be seen in Figures 13–15, which present the comparison between the mass flow rate ( $\dot{m}$ ) that enters the device reservoir during the simulated 600 s due to the incidence of regular and irregular waves, for the points localized in RG, SVP, and TV, respectively.

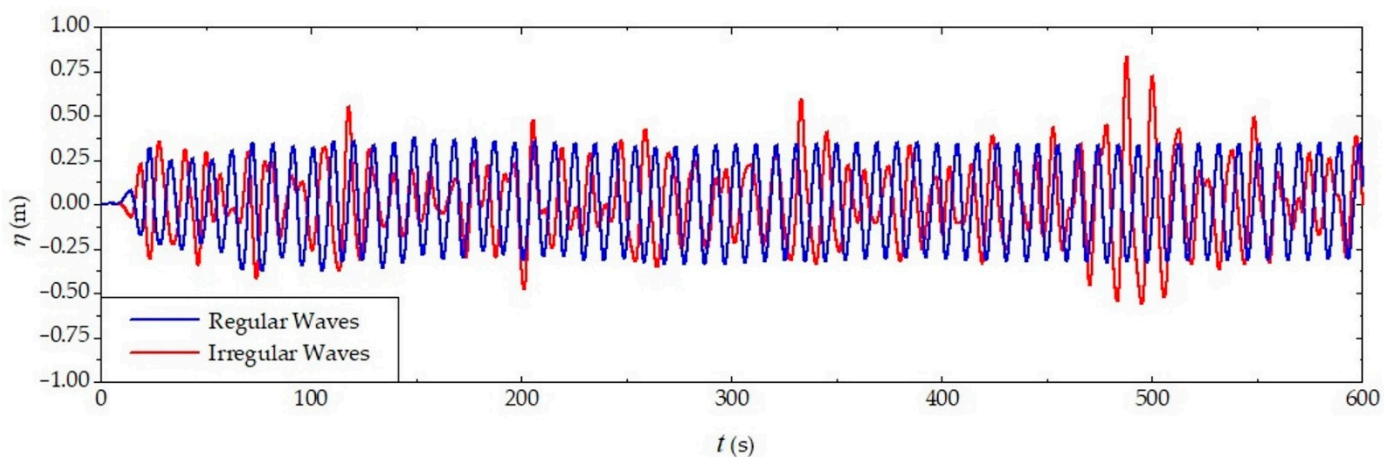


Figure 10. Free-surface elevation obtained with representative regular waves and realistic irregular waves for RG.

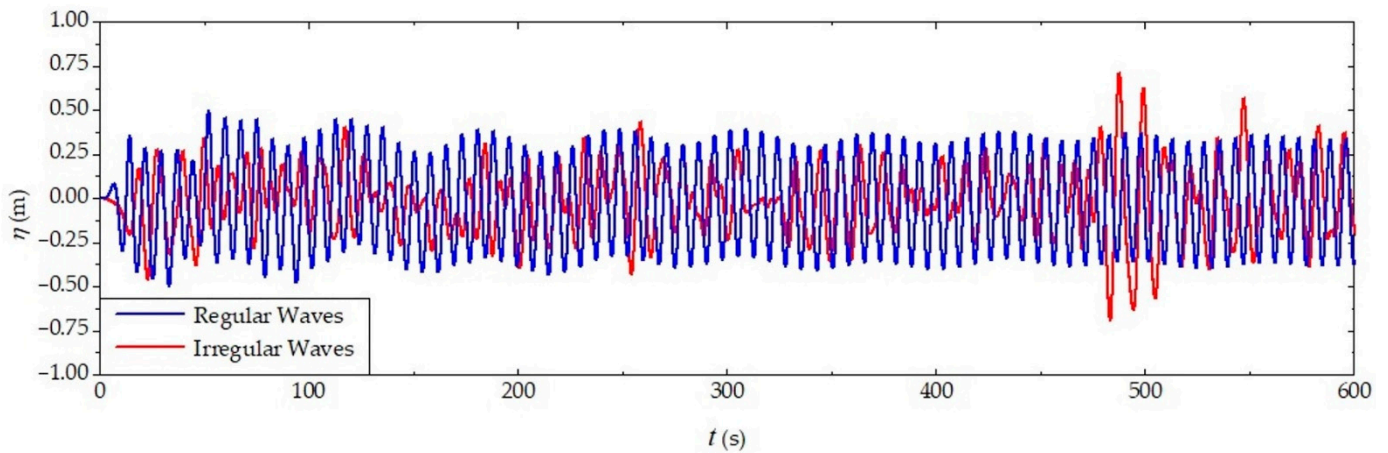


Figure 11. Free-surface elevation obtained with representative regular waves and realistic irregular waves for SVP.

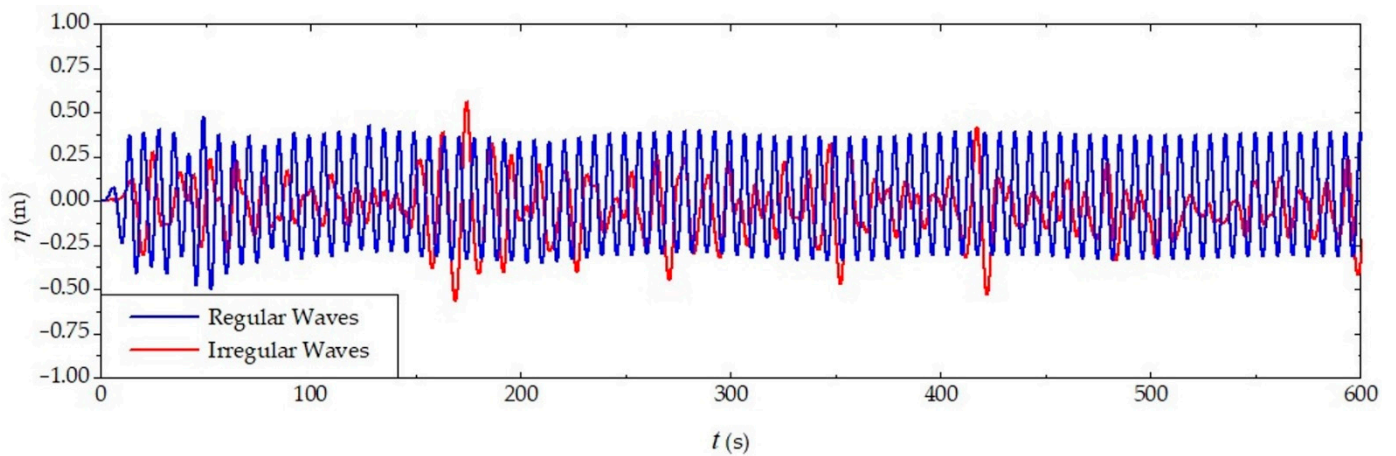


Figure 12. Free-surface elevation obtained with representative regular waves and realistic irregular waves for TV.

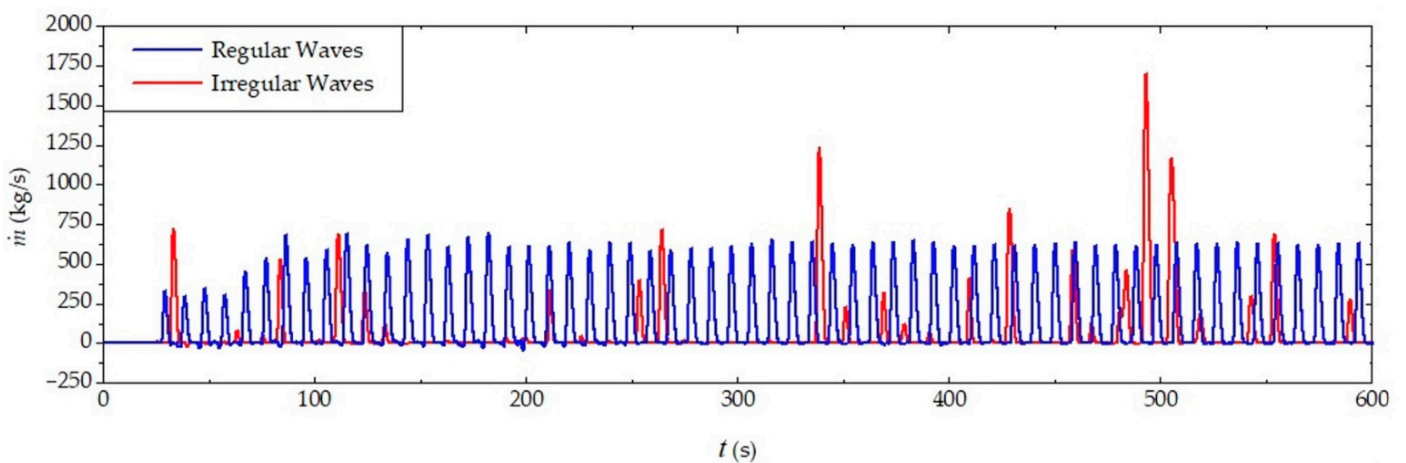
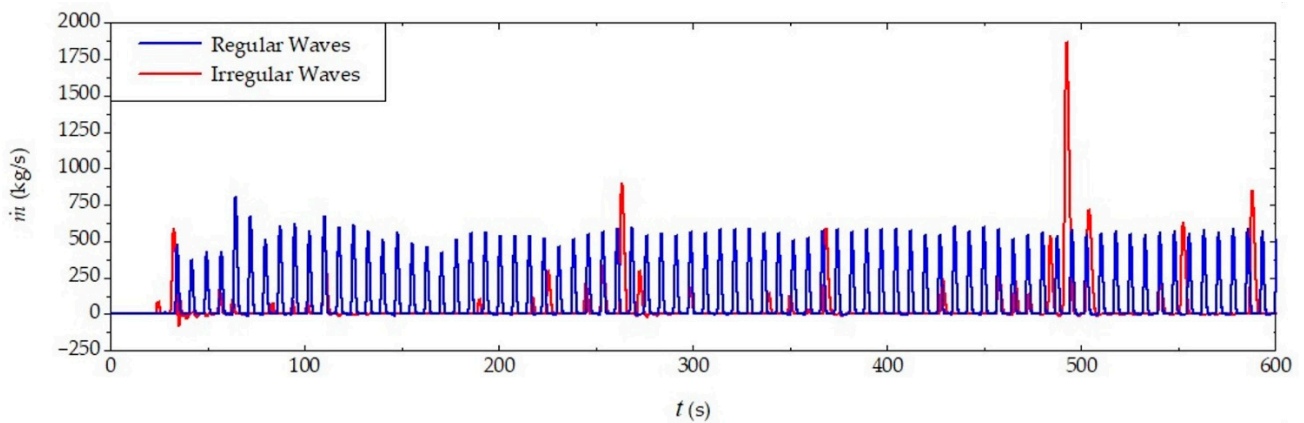
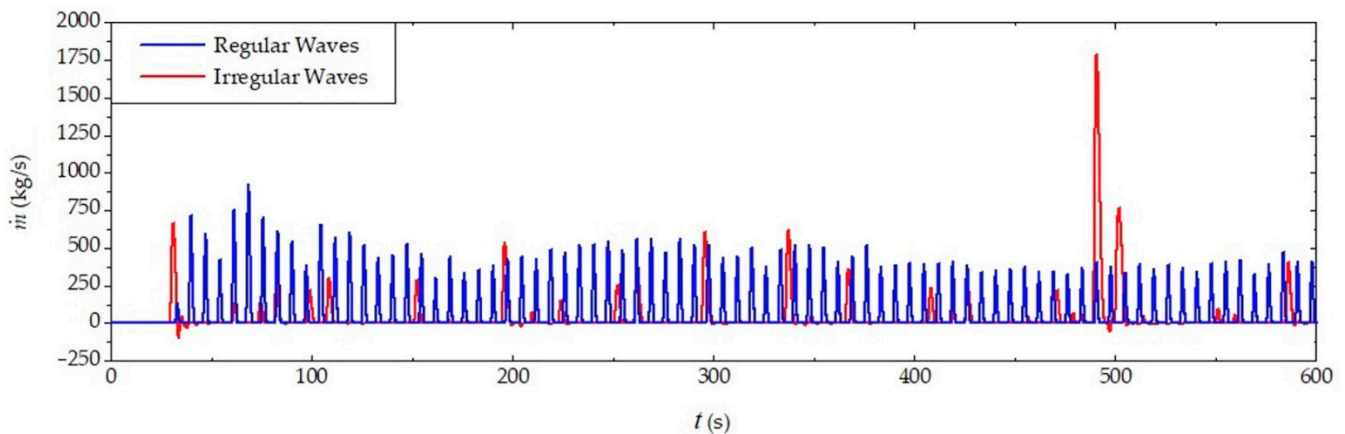


Figure 13. Mass flow rate entering the reservoir due to the incidence of the representative regular waves and realistic irregular waves for RG.



**Figure 14.** Mass flow rate entering the reservoir due to the incidence of the representative regular waves and realistic irregular waves for SVP.



**Figure 15.** Mass flow rate entering the reservoir due to the incidence of the representative regular waves and realistic irregular waves for TV.

Regarding the incidence of representative regular waves on the overtopping WEC, it is possible to observe in Figures 13–15 that before assuming a practically constant behavior of mass flow entering the reservoir, there are lower flow peaks at the simulation start that increase until the stabilization. This fact occurs due to the initial condition of the wave channel, where the fluids are considered in rest, making the first propagated waves smaller than the others, as can be seen at the beginning of the free-surface elevation lines (blue lines) of Figures 10–12.

On the other hand, concerning the incidence of the realistic irregular waves, the occurrence of overtopping and the instantaneous mass flow do not present a stable behavior, as with regular waves. Additionally, it is possible to notice that at several time intervals there was no entry of water into the reservoir, which is explained by the fact that in the realistic sea state there are waves with a shorter period and height and, consequently, less energy, which makes the overtopping of the ramp unfeasible. Finally, it is worth noting that, coincidentally, the highest overtopping peak during the considered 600 s occurred, for all simulated cases, at approximately 500 s.

Figures 16–18 show the variation of water volume ( $V$ ) accumulated in the reservoir of the overtopping device over time due to the incidence of the representative regular waves and realistic irregular waves, respectively, for RG, SVP, and TV. It is possible to observe that for the cases numerically simulated with the representative regular waves, a greater volume of water was accumulated in the reservoir when compared to the cases with the realistic irregular waves, a trend that occurs in all analyzed locations. This behavior is in agreement with the results presented in Figures 13–15.



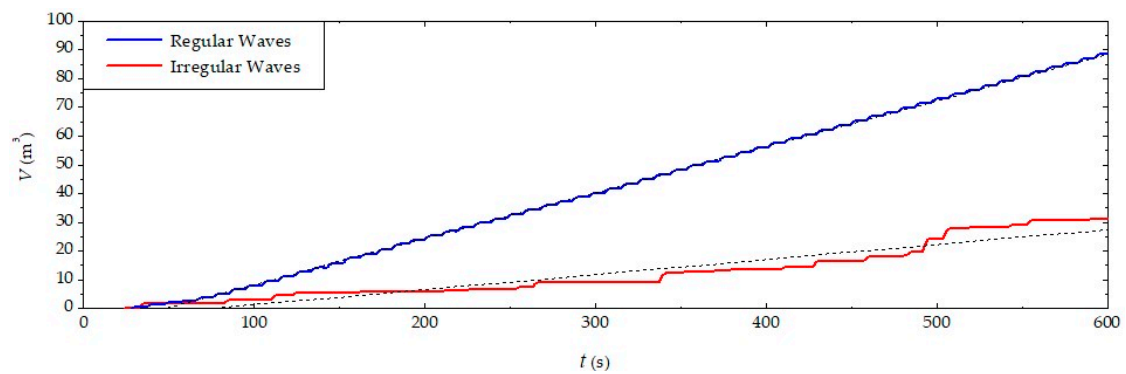


**Figure 16.** Volume of water accumulated in the reservoir over time due to the incidence of the representative regular waves and realistic irregular waves for RG.

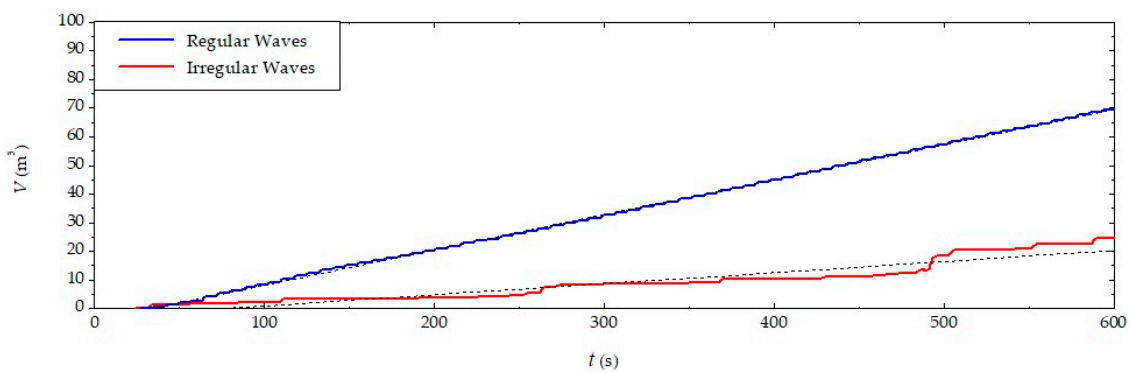


**Figure 17.** Volume of water accumulated in the reservoir over time due to the incidence of the representative regular waves and realistic irregular waves for SVP.

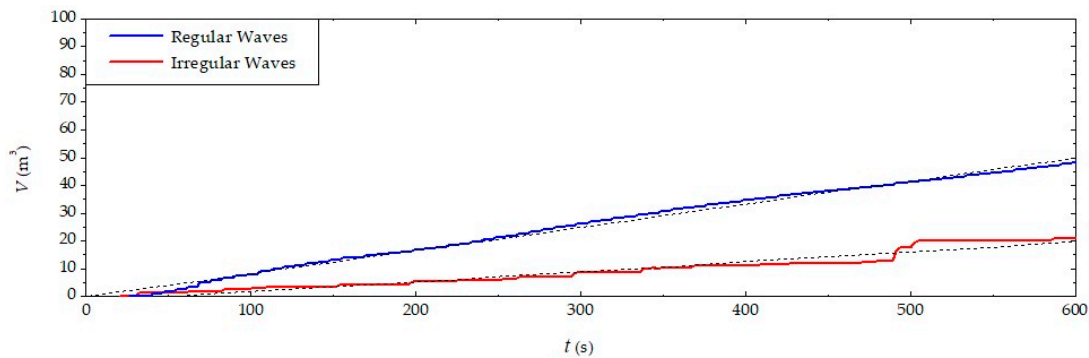


**Figure 18.** Volume of water accumulated in the reservoir over time due to the incidence of the representative regular waves and realistic irregular waves for TV.

Moreover, one can note in Figures 16–18 a fitted curve (black dashed line) to the obtained results for each case. A first-degree polynomial equation for each fitted curve was defined by relating the water volume that enters the reservoir and the elapsed time, characterizing a linear correlation. The correlation coefficient ( $r$ ), or Pearson coefficient, was also obtained, indicating a linear correlation between two variables [49]. Table 3 presents the fitted equation, time range, and Pearson coefficient for all studied cases. The time range covers the interval between the first overtopping and the final simulation time.



**Table 3.** Statistical parameters of curve fitting.

Location	Wave	First-Degree Polynomial	Time Range	<i>r</i>
RG	Regular	$V = 0.1597 \cdot t - 7.5274$	$t \geq 28.0 \text{ s}$	0.9997
	Irregular	$V = 0.0524 \cdot t - 3.8801$	$t \geq 24.0 \text{ s}$	0.9491
SVP	Regular	$V = 0.0123 \cdot t - 4.0325$	$t \geq 26.5 \text{ s}$	0.9998
	Irregular	$V = 0.0384 \cdot t - 2.7831$	$t \geq 24.0 \text{ s}$	0.9456
TV	Regular	$V = 0.0834 \cdot t - 0.0666$	$t \geq 26.0 \text{ s}$	0.9976
	Irregular	$V = 0.0358 \cdot t - 1.8331$	$t \geq 20.5 \text{ s}$	0.9684

From Table 3, one can infer that  $0.95 \leq r \leq 1.00$  represents a strong linear relationship between *V* and *t* [49], allowing the employment of the fitted equations in future investigations considering longer overtopping device uptimes.

In order to quantitatively evaluate the performance of the overtopping device under the incidence of representative regular waves and realistic irregular waves, calculations were performed for the total amount of water accumulated in its reservoir over the 600 s simulated. Table 4 presents these results as volume of water for the evaluated cases.

**Table 4.** Total volume of water accumulated in the reservoir for each case.

Location	Wave	Water Volume (m <sup>3</sup> )
RG	Regular	88.54
	Irregular	31.26
SVP	Regular	69.58
	Irregular	24.51
TV	Regular	48.19
	Irregular	21.08

One can note in Table 4, as well as in Figures 16–18, that for the cases numerically simulated with the representative regular waves, a greater amount of water was accumulated in the reservoir when compared to the cases with the realistic irregular waves, a trend that occurs in all analyzed locations. It was also observed that, although the regular waves representing SVP and TV are identical, the difference in bathymetry and in the depth of the wave channel, of approximately 2.80 m between these cases, influenced the incident water volume in the device reservoir. A possible reason for this is related to the fact that the representative regular wave of SVP propagates in a shallower water layer, which increases the energy flow when compared to the propagation of this same wave in a deeper water layer, as occurs in the case of TV.

Furthermore, an investigation was carried out in order to analyze the fluid–dynamic behavior of the overtopping device aiming to completely fill the reservoir due to the action of regular waves. Thereunto, the case referring to the municipality of RG was simulated for 900 s. Figure 19 shows the maximum mass flow peak that occurred for the representative regular waves (Figure 19a–c) and for the realistic irregular waves (Figure 19d–f), during the simulation with 900 s. The water is represented in red color, while the air is represented in blue color.

As can be seen in Figure 19a,d, respectively, for  $t = 179 \text{ s}$  and  $t = 721 \text{ s}$ , in the instant before the overtopping, a mass of water incident on the device ramp can be observed. After that, in Figure 19b,e, respectively, for  $t = 181 \text{ s}$  and  $t = 725 \text{ s}$ , one can infer that the wave overcame the resistance imposed by the ramp to the flow, climbing it and dropping into the reservoir. It is also noted that the overtopping discharge is greater for the realistic irregular wave (Figure 19e). Finally, Figure 19c,f, respectively, for  $t = 186 \text{ s}$  and  $t = 729 \text{ s}$ , present instants after the overtopping discharges when the water masses return down the ramp at the same time there is an agitation in the water accumulated inside the reservoirs.

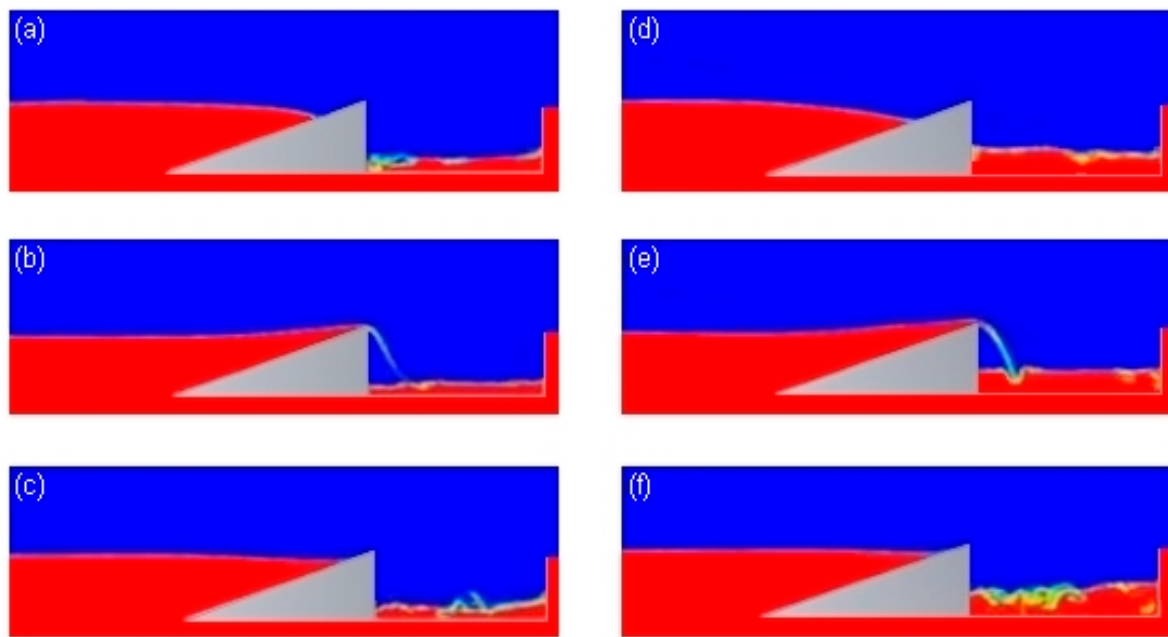


**Figure 19.** Fluid-dynamic behavior during the maximum mass flow peaks referring to the RG coastal region, considering the representative regular waves for (a)  $t = 178$  s; (b)  $t = 182$  s; and (c)  $t = 186$  s; and the realistic irregular waves for (d)  $t = 721$  s; (e)  $t = 725$  s; and (f)  $t = 729$  s.

Still referring to the accumulation of water in the reservoir, Figure 20 presents the phase topology for  $t = 900$  s due to the incidence of representative regular waves (Figure 20a) and realistic irregular waves (Figure 20b). As can be seen in Figure 20a, the reservoir was filled with water for the case that considers the incidence of regular waves. Instead, in Figure 20b, the case that considers the incidence of realistic irregular waves, the reservoir would require the incidence of a significant volume of water until its full filling. Therefore, qualitatively, it is evident that the analysis considering the incidence of regular waves leads to an accumulation of water in the reservoir that is considerably higher than that obtained through the incidence of irregular waves, with this trend quantitatively confirmed in Table 4 and Figures 16–18.

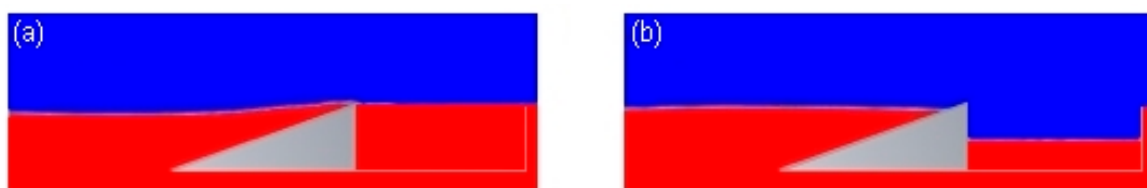


**Figure 20.** Fluid-dynamic behavior referring to the RG coastal region for  $t = 900$  s and considering the incidence of (a) representative regular waves and (b) realistic irregular waves.

Finally, the results obtained here were compared with a previous study by Martins et al. [50], which numerically analyzed the incidence of regular waves (with period of 7.5 s and height of 1 m) and irregular waves from the Pierson–Moskowitz wave spectrum over an onshore overtopping WEC. To do so, only the first 100 s of numerical simulations for RG, SAP, and TV were considered, aiming for an adequate comparison with results of Martins et al. [50]. Table 5 shows the values for the total water amount accumulated inside the reservoirs, with the difference defined by the ratio between the water volumes obtained with regular and irregular waves.

It can be seen in Table 5 that the magnitude of water volumes obtained in Martins et al. [50] is greater (by approximately 2 times) than those of the present work. Taking as reference the regular waves, and considering that their period and wavelength are similar in both studies, one possible reason for this discrepancy is related to the wave high

of 1 m adopted by Martins et al. [50], which is around 50% higher than the representative regular waves of RG and 30% higher than the representative regular waves of SVP and TV. On the other hand, if the difference of accumulated water in each case due to the incidence of regular and irregular waves (see Table 5) is compared, one can observe the same order of magnitude among the cases. Therefore, the present results are in agreement with an analogous previous study.

**Table 5.** Water accumulated in 100 s of simulation.

Case	Wave	Water Volume (m <sup>3</sup> )	Difference (Times)
Present Study—RG	Regular	8.02	2.69
	Irregular	2.98	
Present Study—SVP	Regular	8.34	4.01
	Irregular	2.08	
Present Study—TV	Regular	8.01	2.83
	Irregular	2.83	
Martins et al. [50]	Regular	15.32	3.78
	Pierson–Moskowitz	4.05	

### 5. Conclusions

This present paper compared the operational principle of an overtopping WEC when subjected to the incidence of realistic irregular waves and representative regular waves from sea states located on the coast of the state of Rio Grande do Sul, in southern Brazil. More specifically, the sea states addressed refer to points located in the coastal region of the municipalities of Rio Grande (RG), Santa Vitória do Palmar (SVP), and Tavares (TV).

As expected, the realistic irregular waves showed random peaks of incident mass flow in the device reservoir, while the representative regular waves showed approximately constant mass flow peaks. Still, it was possible to infer that the highest peaks of mass flow achieved for the realistic irregular waves are 2.46, 2.29, and 1.77 times higher than the highest peaks of mass flow reached for the representative regular waves of RG, SVP, and TV, respectively.

Despite having the highest mass flow peaks, some realistic irregular waves do not have enough energy to climb the device ramp. For this reason, the representative regular waves result in a greater water uptake in the device reservoir, as their cyclic behavior and constant height make the overtopping waves occur frequently. With that said, it was concluded that the fluid-dynamic assessment of the incidence of representative regular waves overestimated the water amount accumulated into the reservoir of the overtopping device by approximately 2.83, 2.84, and 2.29 times when considering the cases of RG, SVP, and TV, respectively. These values are in agreement with the previous study of Martins et al. [50].

Moreover, the transient variation of water accumulated in the overtopping reservoir allowed the fitting of curves represented by a first-degree polynomial equation, with strong linear relationship between the water volume and time for each case, which can be used in future studies with no need to run new numerical simulations.

This study showed a considerable difference in the volume of water accumulated in the reservoir of the overtopping device when subjected to representative regular and realistic irregular waves. This fact emphasizes the importance of using realistic sea state data for WEC studies since the irregular waves better represent the sea state of the place where the converter shall be installed. In addition, for future works it is recommended to investigate multi-stage overtopping devices subjected to realistic irregular waves, with the aim of harnessing waves with low energy for its conversion into electricity by means of increasing the water uptake in the reservoir.

**Author Contributions:** Conceptualization: R.G.H., P.H.O., B.N.M. and L.A.I.; methodology: R.G.H., P.H.O., M.d.N.G., L.A.O.R., E.D.d.S., B.N.M. and L.A.I.; software: M.d.N.G., L.A.O.R., E.D.d.S., B.N.M. and L.A.I.; validation: R.G.H., P.H.O., B.N.M. and L.A.I.; formal analysis: R.G.H., M.d.S.P., B.N.M. and L.A.I.; investigation: R.G.H., M.d.S.P., B.N.M. and L.A.I.; resources: C.F., M.d.N.G., L.A.O.R., E.D.d.S. and L.A.I.; data curation: R.G.H. and P.H.O.; writing—original draft preparation: M.d.S.P.; writing—review and editing: R.G.H., M.d.S.P., B.N.M. and L.A.I.; visualization: C.F., M.d.N.G., L.A.O.R. and E.D.d.S.; supervision: L.A.O.R., E.D.d.S., B.N.M. and L.A.I.; project administration: L.A.O.R., E.D.d.S., B.N.M. and L.A.I.; funding acquisition: C.F., M.d.N.G., L.A.O.R., E.D.d.S. and L.A.I. All authors have read and agreed to the published version of the manuscript.

**Funding:** This research was funded by the Brazilian Coordination for the Improvement of Higher Education Personnel—CAPES (Finance Code 001), Research Support Foundation of the State of Rio Grande do Sul—FAPERGS (Public Call FAPERGS 07/2021—*Programa Pesquisador Gaúcho*—PqG—21/2551-0002231-0), and Brazilian National Council for Scientific and Technological Development—CNPq (Processes: 309648/2021-1, 307791/2019-0, 308396/2021-9, 440010/2019-5, and 440020/2019-0), and the Ministry of Science, Technology, Innovation and Communications (Public Call MCTIC/CNPq N°28/2018—Universal).

**Institutional Review Board Statement:** Not applicable.

**Informed Consent Statement:** Not applicable.

**Data Availability Statement:** The data presented in this study are available on request from the corresponding author. The data are not publicly available due to privacy reasons.

**Acknowledgments:** The authors thank FAPERGS (Public Call FAPERGS 07/2021—*Programa Pesquisador Gaúcho*—PqG—process: 21/2551-0002231-0) and CNPq (Public Call CNPQ/EQUINOR *Energia Ltda* N° 38/2018—Processes: 440010/2019-5 and 440020/2019-0) for the financial support. R.G.H. thanks CNPq for his master's scholarship. P.H.O. and M.d.S.P. thank CAPES (Finance Code 001) for their master's scholarship. The author M.d.N.G. thanks MCTIC (Public Call MCTIC/CNPq N° 28/2018—Universal). The authors L.A.O.R., E.D.d.S., and L.A. Isoldi are grant holders of the CNPq (processes: 307791/2019-0, 308396/2021-9, and 309648/2021-1, respectively).

**Conflicts of Interest:** The authors declare no conflict of interest. The funders had no role in the design of the study; in the collection, analyses, or interpretation of data; in the writing of the manuscript, or in the decision to publish the results.

## Notes

<sup>1</sup> <https://www.marinha.mil.br/chm/dados-do-segnav-cartas-nauticas/cartas-nauticas>.

## References

- Fontana, R.L.M.; Costa, S.S.; Silva, J.A.B.; Rodrigues, A.J. Teorias Demográficas e o Crescimento Populacional no Mundo. *Cadernos de Graduação. Ciências Hum. E Sociais Unit* **2015**, *2*, 113–124.
- REN21. *Renewables 2019: Global Status Report*; REN21: Paris, France, 2019.
- Gunn, K.; Stock-Williams, C. Quantifying the global wave power resource. *Renew. Energy* **2012**, *44*, 296–304. [[CrossRef](#)]
- Espindola, R.L.; Araújo, A.M. Wave energy resource of Brazil: An analysis from 35 years of ERA—Interim reanalysis data. *PLoS ONE* **2017**, *12*, e0183501. [[CrossRef](#)] [[PubMed](#)]
- Pecher, A.; Kofoed, J.P. *Handbook of Ocean Wave Energy*; Springer: Cham, Switzerland, 2017.
- Jungrungruengtaworn, S.; Hyun, B.-S. Influence of Slot Width on the Performance of Multi-Stage Overtopping Wave Energy Converters. *Int. J. Nav. Archit. Ocean Eng.* **2017**, *9*, 668–676. [[CrossRef](#)]
- Han, Z.; Liu, Z.; Shi, H. Numerical study on overtopping performance of a multi-level breakwater for wave energy conversion. *Ocean Eng.* **2018**, *150*, 94–101. [[CrossRef](#)]
- Liu, Z.; Han, Z.; Shi, H.; Yang, W. Experimental study on multi-level overtopping wave energy convertor under regular wave conditions. *Int. J. Nav. Archit. Ocean Eng.* **2018**, *10*, 651–659. [[CrossRef](#)]
- Martins, J.C.; Goulart, M.M.; das Gomes, M.N.; Souza, J.A.; Rocha, L.A.O.; Isoldi, L.A.; Dos Santos, E.D. Geometric evaluation of the main operational principle of an overtopping wave energy converter by means of Constructal Design. *Renew. Energy* **2018**, *118*, 727–741. [[CrossRef](#)]
- Palma, G.; Formentin, S.M.; Zanuttigh, B.; Contestabile, P.; Vicinanza, D. Numerical Simulations of the Hydraulic Performance of a Breakwater-Integrated Overtopping Wave Energy Converter. *J. Mar. Sci. Eng.* **2019**, *7*, 38. [[CrossRef](#)]
- Di Lauro, E.; Lara, J.L.; Maza, M.; Losada, I.J.; Contestabile, P.; Vicinanza, D. Stability analysis of a non-conventional breakwater for wave energy conversion. *Coast. Eng.* **2019**, *145*, 36–52. [[CrossRef](#)]

12. Di Lauro, E.; Maza, M.; Lara, J.L.; Losada, I.J.; Contestabile, P.; Vicinanza, D. Advantages of an innovative vertical breakwater with an overtopping wave energy converter. *Coast. Eng.* **2020**, *159*, 103713. [[CrossRef](#)]
13. Martins, J.C.; Fragassa, C.; Goulart, M.M.; dos Santos, E.D.; Isoldi, L.A.; das Neves Gomes, M.; Rocha, L.A.O. Constructural Design of an Overtopping Wave Energy Converter Incorporated in a Breakwater. *J. Mar. Sci. Eng.* **2022**, *10*, 471. [[CrossRef](#)]
14. Liu, Z.; Shi, H.; Cui, Y.; Kim, K. Experimental study on overtopping performance of a circular ramp wave energy converter. *Renew. Energy* **2017**, *104*, 163–176. [[CrossRef](#)]
15. Barbosa, D.V.E.; Santos, A.L.G.; Dos Santos, E.D.; Souza, J.A. Overtopping device numerical study: Openfoam solution verification and evaluation of curved ramps performances. *Int. J. Heat Mass Transf.* **2019**, *131*, 411–423. [[CrossRef](#)]
16. Contestabile, P.; Crispino, G.; Russo, S.; Gisonni, C.; Cascetta, F.; Vicinanza, D. Crown wall modifications as response to wave overtopping under a future sea level scenario: An experimental parametric study for an innovative composite seawall. *Appl. Sci.* **2020**, *10*, 2227. [[CrossRef](#)]
17. Mariani, A.; Crispino, G.; Contestabile, P.; Cascetta, F.; Gisonni, C.; Vicinanza, D.; Unich, A. Optimization of Low Head Axial-Flow Turbines for an Overtopping BReakwater for Energy Conversion: A Case Study. *Energies* **2021**, *14*, 4618. [[CrossRef](#)]
18. Machado, B.N.; Oleinik, P.H.; Kirinus, E.P.; Dos Santos, E.D.; Rocha, L.A.O.; Das Gomes, M.N.; Conde, J.M.P.; Isoldi, L.A. WaveMIMO Methodology: Numerical Wave Generation of a Realistic Sea State. *J. Appl. Comput. Mech.* **2021**, *1*, 2129–2148. [[CrossRef](#)]
19. Taboada, J.V.; Casás, V.D.; Yu, X.; Gemilang, G.M.; Sampaio, P. Study review of the electrical power generation: Wave energy converting device system from the swell. *IOP Conf. Ser. Mater. Sci. Eng.* **2021**, *1201*, 012001. [[CrossRef](#)]
20. Chen, G.; Chapron, B.; Ezraty, R.; Vandemark, D. A Global View of Swell and Wind Sea Climate in the Ocean by Satellite Altimeter and Scatterometer. *J. Atmos. Ocean. Technol.* **2002**, *19*, 1849–1859. [[CrossRef](#)]
21. Kharati-Koopae, M.; Kiali-Kooshkghazi, M. Assessment of plate-length effect on the performance of the horizontal plate wave energy converter. *J. Waterw. Port Coast. Ocean Eng.* **2019**, *145*, 04018037. [[CrossRef](#)]
22. Seibt, F.M.; Camargo, F.V.; Dos Santos, E.D.; Neves, G.M.; Rocha, L.A.O.; Isoldi, L.A.; Fragassa, C. Numerical evaluation on the efficiency of the submerged horizontal plate type wave energy converter. *FME Trans.* **2019**, *47*, 543–551. [[CrossRef](#)]
23. Chakraborty, T.; Majumder, M. Impact of extreme events on conversion efficiency of wave energy converter. *Energy Sci. Eng.* **2020**, *8*, 3441–3456. [[CrossRef](#)]
24. Kralli, V.-E.; Theodossiou, N.; Karambas, T. Optimal Design of Overtopping Breakwater for Energy Conversion (OBREC) Systems Using the Harmony Search Algorithm. *Front. Energy Res.* **2019**, *7*, 80. [[CrossRef](#)]
25. Zabihi, M.; Mazaheri, S.; Rezaee Mazyak, A. Wave Generation in a Numerical Wave Tank. *Int. J. Coast. Offshore Eng.* **2017**, *5*, 25–35.
26. Machado, B.N.; Kisner, E.V.; Paiva, M.S.; Gomes, M.N.; Rocha, L.A.O.; Marques, W.C.; Santos, E.D.; Isoldi, L.A. Numerical Generation of Regular Waves Using Discrete Analytical Data as Boundary Condition of Prescribed Velocity. In Proceedings of the XXXVIII Iberian Latin-American Congress on Computational Methods in Engineering, Rio de Janeiro, Brazil, 5–8 November 2017.
27. Machado, F.M.M.; Lopes, A.M.G.; Ferreira, A.D. Numerical simulation of regular waves: Optimization of a numerical wave tank. *Ocean Eng.* **2018**, *170*, 89–99. [[CrossRef](#)]
28. Finnegan, W.; Goggins, J. Linear irregular wave generation in a numerical wave tank. *Appl. Ocean Res.* **2015**, *52*, 188–200. [[CrossRef](#)]
29. Higuera, P.; Lara, J.L.; Losada, I.J. Realistic wave generation and active wave absorption for Navier–stokes models. *Coast. Eng.* **2013**, *71*, 102–118. [[CrossRef](#)]
30. Higuera, P.; Lara, J.L.; Losada, I.J. Simulating coastal engineering processes with OpenFOAM®. *Coast. Eng.* **2013**, *71*, 119–134. [[CrossRef](#)]
31. Patankar, S.V. *Numerical Heat Transfer and Fluid Flow*; McGraw Hill: New York, NY, USA, 1980.
32. Versteeg, H.K.; Malalasekera, W. *An Introduction to Computational Fluid Dynamics: The Finite Volume Method*, 2nd ed.; Pearson Education: London, UK, 2007.
33. Hirt, C.W.; Nichols, B.D. Volume of Fluid (VOF) Method for the Dynamics of Free Boundaries. *J. Comput. Phys.* **1981**, *39*, 201–225. [[CrossRef](#)]
34. Schlichting, H. *Boundary Layer Theory*, 7th ed.; McGraw-Hill: New York, NY, USA, 1979.
35. Foyhirun, C.; Kositgittiwong, D.; Ekkawatpanit, C. Wave energy potential and simulation on the Andaman sea coast of Thailand. *Sustainability* **2020**, *12*, 3657. [[CrossRef](#)]
36. Lisboa, R.C.; Teixeira, P.R.; Didier, E. Regular and irregular wave propagation analysis in a flume with numerical beach using a Navier-stokes based model. *Defect Diffus. Forum* **2017**, *372*, 81–90. [[CrossRef](#)]
37. Awk, T. *TOMAWAC User Manual Version 7.2. 7.2.3*; The Telemac-Mascaret Consortium: Chatou, France, 2017.
38. Maciel, R.P.; Fragassa, C.; Machado, B.N.; Rocha, L.A.O.; Dos Santos, E.D.; Das Gomes, M.N.; Isoldi, L.A. Verification and Validation of a Methodology to Numerically Generate Waves Using Transient Discrete Data as Prescribed Velocity Boundary Condition. *J. Mar. Sci. Eng.* **2021**, *9*, 896. [[CrossRef](#)]
39. Oleinik, P.H.; Tavares, G.P.; Machado, B.N.; Isoldi, L.A. Transformation of water wave spectra into time series of surface elevation. *Earth* **2021**, *2*, 997–1005. [[CrossRef](#)]
40. Airy, G.B. *Tides and Waves*; Encyclopædia Metropolitana: London, UK, 1845.
41. Dean, R.G.; Dalrymple, R.A. *Water Wave Mechanics for Engineers and Scientists*; World Scientific: Singapore, 1991; Volume 2.
42. Chakrabarti, S.K. *Handbook of Offshore Engineering*; Elsevier: Chicago, IL, USA, 2005.
43. Liu, Z.; Hyun, B.S.; Hong, K. Numerical study of air chamber for oscillating water column wave energy converter. *China Ocean Eng.* **2011**, *25*, 169–178. [[CrossRef](#)]



44. Gomes, M.; Das, N.; Lorenzini, G.; Rocha, L.A.O.; Dos Santos, E.D.; Isoldi, L.A. Constructal Design Applied to the Geometric Evaluation of an Oscillating Water Column Wave Energy Converter Considering Different Real Scale Wave Periods. *J. Eng. Thermophys.* **2018**, *27*, 173–190. [[CrossRef](#)]
45. ANSYS. *ANSYS Fluent Theory Guide, Release 18.2*; ANSYS Inc.: Canonsburg, PA, USA, 2017.
46. Khaware, A.; Gupta, V.; Srikanth, K.; Sharkey, P. Sensitivity Analysis of Non-linear Steep Waves using VOF Method. In Proceedings of the Tenth International Conference on Computational Fluid Dynamics (ICCFD10), Barcelona, Spain, 9–13 July 2018.
47. Kisner, E.V.; Machado, B.N.; Dos Santos, E.D.; Rocha, L.A.O.; Das Gomes, M.N.; Isoldi, L.A. Proposta de malha Stretched para ser utilizada com o método de imposição de dados discretos como condição de contorno de velocidade prescrita na geração numérica de ondas. *Sci. Plena* **2019**, *15*, 1–9. [[CrossRef](#)]
48. Saincher, S.; Banerjee, J. Design of a numerical wave tank and wave flume for low steepness waves in deep and intermediate water. *Procedia Eng.* **2015**, *116*, 221–228. [[CrossRef](#)]
49. Schiefer, H.; Schiefer, F. *Statistics for Engineers—An Introduction with Examples from Practice*; Springer: Wiesbaden, Germany, 2021.
50. Martins, J.C.; Goulart, M.M.; Gomes, M.N.; Souza, J.A.; Rocha, L.A.O.; Isoldi, L.A.; Dos Santos, E.D. Análise Numérica de um Dispositivo de Galgamento Onshore Comparando a Influência de uma onda monocromática e de um Espectro de Ondas. *Rev. Bras. Energ. Renov.* **2017**, *6*, 472–488. [[CrossRef](#)]